

UNIVERSITY COLLEGE LONDON

Overcoming Data Scarcity in Scanning Tunnelling Microscopy Image Segmentation

**Nikola L. Kolev^{1,2,*}, Max Trouton^{1,4}, Filippo Federici Canova^{5,6},
Geoff Thornton^{1,4}, David Z. Gao^{3,5,7}, Neil J. Curson^{1,2},
Taylor J. Z. Stock^{1,2,*}**

¹London Centre for Nanotechnology,
University College London, 17-19 Gordon Street, London, WC1H 0AH, UK

²Department of Electronic and Electrical Engineering,
University College London,
London, WC1E 7JE, UK

³Department of Physics and Astronomy, University College London, London, WC1E 7JE, UK

⁴Department of Chemistry, University College London,
London, WC1E 7JE, UK

⁵Aalto Science Institute, School of Science, Aalto University, 02150 Espoo, Finland

⁶Nanolayers Research Computing LTD,
London, UK

⁷Department of Physics,
NTNU Norwegian University of Science and Technology,
Trondheim, Norway

* Authors to whom any correspondence should be addressed.

Abstract

Scanning tunnelling microscopy (STM) is a powerful technique for imaging surfaces with atomic resolution, providing insight into physical and chemical processes at the level of single atoms and molecules. A regular task of STM image analysis is the identification and labelling of features of interest against a uniform background. Performing this manually is a labour-intensive task, requiring significant human effort. To reduce this burden, we propose an automated approach to the segmentation of STM images that uses both few-shot learning and unsupervised learning. Our technique offers greater flexibility compared to previous supervised methods; it removes the requirement for large manually annotated datasets and is thus easier to adapt to an unseen surface while still maintaining a high accuracy. We demonstrate the effectiveness of our approach by using it to recognise atomic features on three distinct surfaces: Si(001), Ge(001), and TiO₂(110), including adsorbed AsH₃ molecules on the silicon and germanium surfaces. Our model exhibits strong generalisation capabilities, and following initial training, can be adapted to unseen surfaces with as few as one additional labelled data point. This work is a significant step towards efficient and material-agnostic, automatic segmentation of STM images.

June 13, 2025

1 Introduction

A scanning probe microscopy (SPM) image is a dense $n \times n$ matrix of values, recording the point wise interaction between an atomically sharp probing tip and the atoms on a surface. In the case of scanning tunnelling microscopy (STM) [4], the measured tunnelling electron current between tip and surface relates directly to the tip-sample separation and the local density of electronic states of the surface. An STM image therefore contains both topographic and electronic information. Given this complexity, the quantitative analysis of STM results requires correlation between the images and physical models of the measured system. In practice, this is achieved by comparing the results of theoretical studies with significant quantities of labelled STM data. Computer vision, the ability for computers to derive information from images, can be used to automate much of this procedure, and machine learning (ML) based image recognition finds a natural application in the analysis and segmentation of STM images.

In existing work, Rashidi et al., and Ziatdinov et al. have both successfully trained convolutional neural networks (CNN) to detect a variety of known defects in STM images of the hydrogen terminated silicon surface [47] [29]. Additionally, the exploration of machine learning (ML) for real-time image improvement by automated STM tip monitoring, modification, and repair, has shown promising initial results and bodes well for the broader application of ML for task automation in the STM community [30] [10] [22] [11]. Despite these successes, a notable limitation of existing applications of ML to STM is its reliance on foreknowledge of the measured surfaces. STM is regularly applied to new materials and novel experiments inherently give rise to novel data. However, accurate analysis using traditional supervised machine learning techniques, such as those used in [29] [30] [10], requires significant amounts of labelled training data for each newly studied surface system. For example, the classification problems in references [30] and [10] use around 3000 labelled STM images, but training data sets of this size may not be practical or even possible in other STM applications. This limitation can reduce or even remove the advantages offered by using ML for data labelling.

One possible solution to this problem is the artificial synthesis of labelled data. This can, in princi-

ple, be accomplished with density functional theory (DFT) [7], but in practice this approach often requires the introduction of additional neural networks to address dissimilarities between theoretical and experimental data [21] [19] [48], not to mention the need for an expert in DFT calculations and many hours of computational resources. A more straightforward solution, to the onerous demand for extensive labelled data, is an ML image recognition technique for STM that relies on little or no data from unseen material systems. In the approach presented here, we minimise the number of labelled examples required from each new experiment by using a combination of unsupervised learning and few shot learning (FSL) [37].

FSL is a widely used image recognition technique that has also been adapted for other modalities where human discernment typically excels, such as audio, language, and radar [16] [26] [23]. Rather than learning to classify an object into several predetermined classes, FSL networks learn what it means for two objects to be the same. Training of an FSL model focuses on differentiating between two or more inputs, rather than classifying them, and this lifts the requirement for large training datasets. While initial training can still require large amounts of data (a few hundred labelled data points in our work), once completed, new problems can be successfully tackled with as little as one labelled data point per class [37].

Despite its flexibility, to our knowledge, FSL has not yet been utilised in STM or in the broader SPM community. Notably, it has gained attention within the astronomy community for classifying galaxy morphologies [46], an arguably similar task to the one posed by STM data. FSL has also seen recent application in electron microscopy where it has been used for coarse segmentation of scanning transmission electron microscopy (STEM) images of epitaxial heterostructures [1], and space group classification of electron backscatter diffraction (EBSD) patterns [20]. In addition, although not strictly FSL, the MicroNet microscopy dataset, has been used to demonstrate accurate electron microscopy image segmentation using decoders trained on only a few fully segmented images [39]. These successes in related fields suggest that FSL approaches may also be beneficial when applied to STM data.

In our work, we apply FSL to the STM study of atomic-scale defects on semiconductor surfaces. This is motivated by the technological importance

of dopant precursor chemistry on the Si(001) and Ge(001) surfaces, which has applications in quantum computing [44] [31]. When paired with hydrogen lithography (an atomically precise STM-based fabrication technique) [25], suitable dopant precursors allow for the creation of atomic-scale quantum electronic devices, including dopant-spin based qubits [42] [6]. To date, single atom devices have been fabricated in this way using phosphine and phosphorus in silicon, but new precursors for dopants such as arsenic and boron have been established [38] [34] [12]. The STM experiments that are used to assess candidate precursors, examine the chemistry of new molecules on known surfaces. Having an ML tool that can easily adapt to STM data of new precursors and dopants, continually building upon the existing knowledge from past experiments, will help to speed the process of discovering suitable new precursors.

Compared to the examples of FSL in electron microscopies cited above, we not only develop an effective FSL approach for our test case STM data, but we also assess the suitability of different FSL algorithms for STM data analysis. Here, we investigate four different FSL algorithms: prototypical [35], matching [41], relation [40], and simple shot [43], and find the prototypical network performs best, overall, with up to 94% accuracy in our test cases. Finally, we also compare pretrained networks with networks trained in-house on subject specific data and explore how the number of classes in a training set can improve the accuracies of our networks. By evaluating several of the most popular FSL networks in this way, we aim to provide a guide for others in the SPM community and related fields who wish to apply FSL to their microscopy data.

2 Background

One routine application of STM is the exploration of surface chemical reactions. In these experiments, STM data reveals atomic scale features present on a surface before and after exposure to adsorbates. The larger the area one examines with the STM, the higher the statistical significance of the findings. Therefore, from an image recognition perspective, the task at hand is to identify and label all atomic-scale features in many similar images. As a specific example of this, Figures 1(a) and (b) present filled state (tunnelling from the sample) and empty state (tunnelling to the

sample) STM images of a hydrogen terminated silicon surface: Si(001):H.

When working with a known substrate and a new adsorbate, such as Si(001) and the terminating hydrogen in our example, the features will broadly divide into two classes: known native defects of the substrate, and new features attributed to the adsorbate. Traditionally, an STM user would sift through the data, labelling every instance of previously unseen defects and then attribute these to the new chemical species. This is illustrated in Figures 1(a) and 1(b), where coloured boxes are used to label native defects such as bright and dark silicon atomic vacancies, as well as features associated with the hydrogen termination, such as single and double dangling bonds and siloxane (adsorbed oxygen from background water). Examples of a double dangling bond and a siloxane feature are shown in detail in Figures 1(c), and 1(d), respectively [8]. The identified features are distinguished from a uniform background, and in the case of Si(001):H, this background is composed of atomic dimer rows, shown in detail in Figure 1(e). Finally, in addition to identifiable feature types, there may also be anomalies present. These are defects that do not fit into any class, and which appear only once or twice in the data. Due to their scarcity, anomalies are usually dismissed during counting or included in uncertainties. An ML based approach to labelling data of this sort should be capable of handling both broad feature classes, known substrate defects and new adsorbate features, plus any anomalies.

To demonstrate our FSL based STM image recognition approach, we first train the networks using data from silicon surfaces, that is, Si(001):H shown in Figure 1(a) and (b), both with and without adsorbed AsH₃ molecules, plus data from the bare Si(001) shown in Figure 1(f). With the models trained, we then address two additional surfaces: arsine adsorbed germanium: Ge(001):AsH₃, and titania: TiO₂(110), examples of which are shown in Figures 1(g) and 1(h), respectively. While germanium’s structure and semiconductor properties are very similar to those of silicon, the well-studied titania surface [3] [27] [9] is different from the group IV semiconductor surfaces, in both appearance and structure, so that our three test cases represent a gradual progression from familiar to unfamiliar.

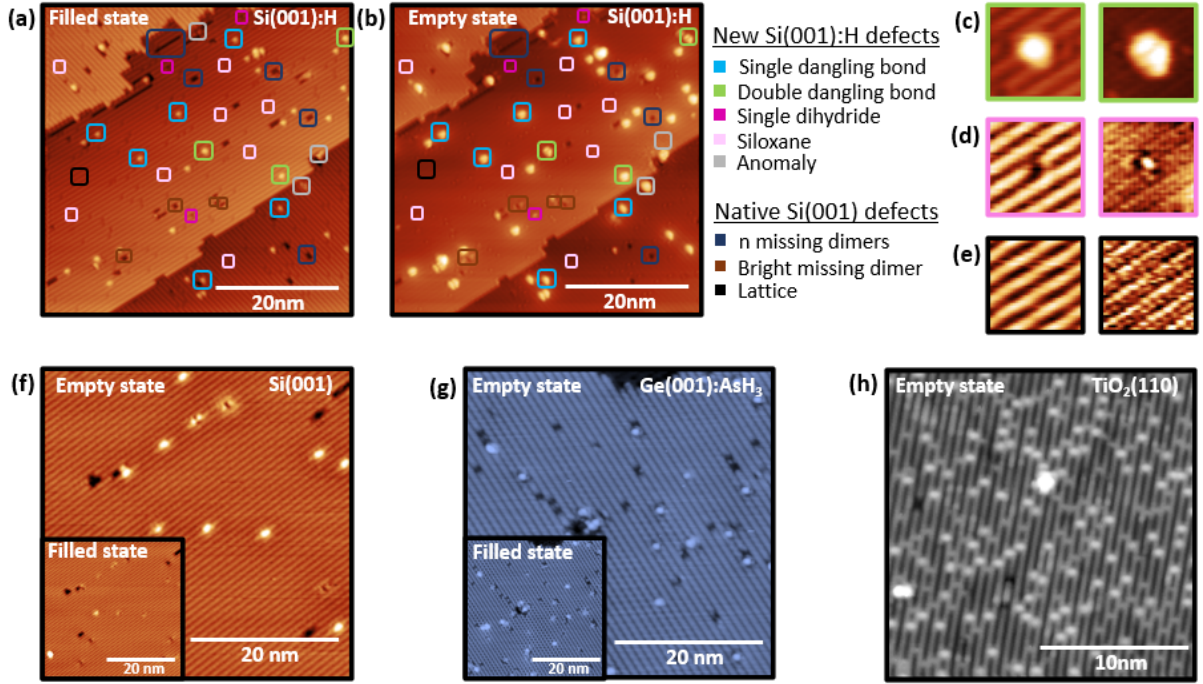


Figure 1: (a) Filled and (b) empty state STM images of the same area of a Si(001):H surface. Imaging parameters: -2 V/+2 V, 50 pA. Different defect types are circled with different colours. Not all defects have been labelled to avoid overcrowding. (c)-(e) show cropped features from (a) and (b). (c) A double dangling bond (i.e. an exposed bare silicon dimer on the Si(001):H surface). (d) A siloxane feature (oxygen atom bridging a silicon dimer: Si-O-Si). (e) Detail of the hydrogen terminated silicon dimer rows. (f) Filled and empty state STM images of the Si(001) surface. Imaging parameters +2 V/-2 V, and 50 pA. (g) Filled and empty state images of the Ge(001):AsH₃ surface. Imaging parameters: -1.5 V/+1.0 V, 200 pA (h) Empty state STM image of the TiO₂ (110) surface. Imaging parameters: +1.6 V, 100 pA. All images are plane-levelled and scan line aligned.

3 Method

3.1 Image Recognition Workflow

Figure 2 presents an overview of our approach to FSL-based image recognition for STM data segmentation. Here we use the Ge(001):AsH₃ system of Figure 1(f) as an example. The workflow consists of five steps.

(i) Data acquisition and pre-processing

STM images are acquired in two channels (filled and empty states), then distortion corrected, aligned, and combined in image tensors that are fed forward through the image processing framework.

(ii) U-Net binary segmentation

The unseen data is coarsely segmented by a U-Net, each pixel is labelled either as defect or lattice. The U-Net module requires training data for each new substrate, and this is provided using an unsupervised

learning module for data labelling, described below in section 3.3.

(iii) Feature cropping

The atomic defects identified in step (ii) are then isolated in uniform image crops that are resampled to match network dimensionality, before feeding forward to the FSL module.

(iv) User defined N-way K-shot problem

The user defines N feature classes, and labels K examples for each class using images from the set of crops collected in step (iii), thus generating the support set required by the FSL network. Within this step, the support set can be changed from one set of images to another, and anomalies may be excluded from analysis as the STM experiment progresses and the character of the data develops.

(v) FSL classification

Finally, with the support set established, the FSL network runs inference on the remaining unseen

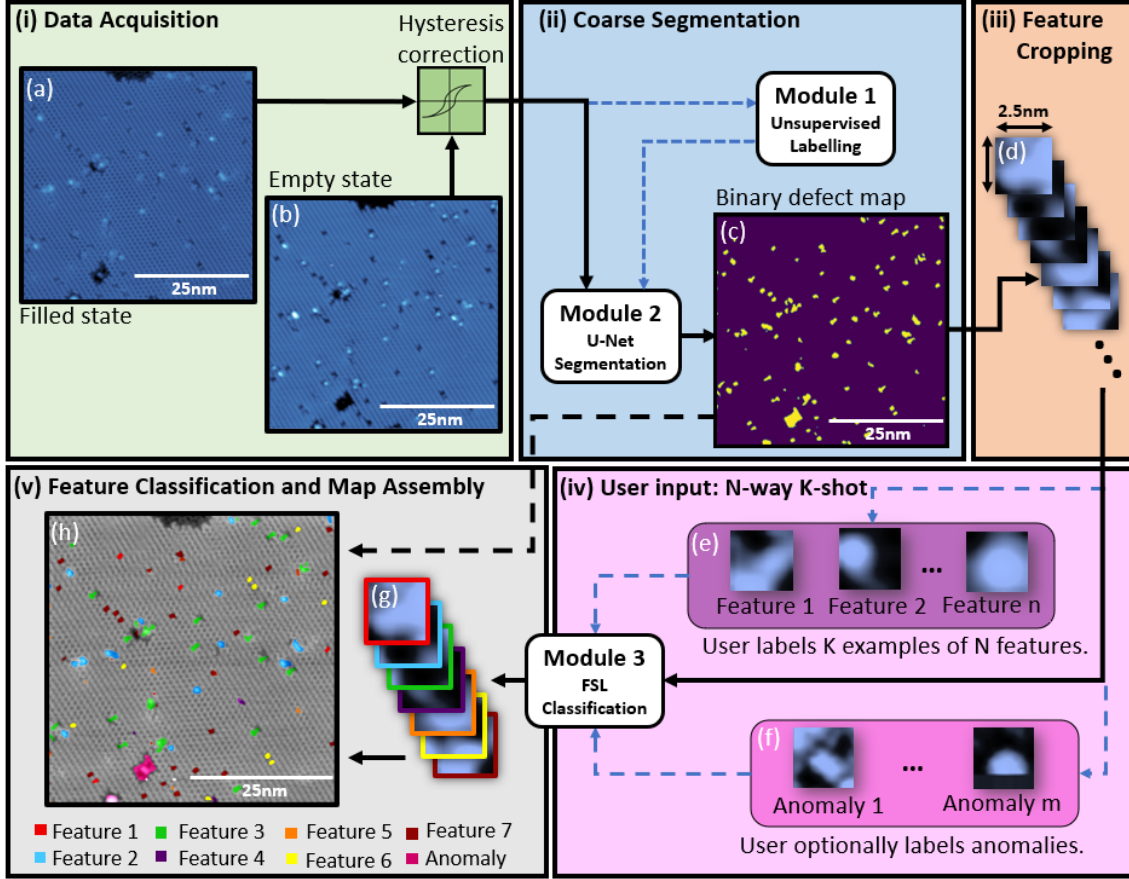


Figure 2: STM Image Segmentation and Feature Classification Workflow: The workflow is illustrated using filled and empty state data, (a) and (b), from the Ge(001):AsH₃ system. It is divided into 5 steps (i through v) and utilizes three image processing modules (1 through 3). Step (i) STM data acquisition and pre-processing including hysteresis correction. (ii) Course segmentation by a U-Net (Module 2) to produce a binary map (c). The U-Net is trained on data labelled using an unsupervised clustering technique (Module 1). (iii) Atomic defects identified in step ii are isolated in uniform cropped images (d) and resampled to match network dimensionality. (iv) The FSL support set (e) is generated by the user who defines N feature classes and labels K examples for each class using a subset of crops from step (iii). The user may also exclude anomalous features (f) from analysis at this step. (v) Using the support set defined in step (iv), the FSL network (Module 3) sorts all remaining unseen cropped features into the N classes. Finally, classified features of interest (g) are combined with the binary map (c) into the final output of an STM image feature map (h).

cropped features, sorting them into the N user defined classes. Once all features of interest have been classified, this information is combined with the course segmentation of step (ii), producing the final output, a segmented image with full classification of all atomic scale features of interest.

3.2 Module 1: Unsupervised Labelling

To produce accurate coarse segmentations in step (ii) above we require multiple new labelled scans to train

the U-Net for new substrates. Although our results demonstrate that as few as five scans can be sufficient, this still takes considerable time for a single person to annotate. To significantly reduce this burden, we utilize unsupervised learning to produce the labelled training data for the U-Net. Our approach here is similar to that developed by Archit et al. [2], using large pretrained models. The key difference is that we do not use the output of the pretrained models to fine-tune a new large model but instead train a smaller model capable of segmenting images on a CPU in seconds - in effect distilling the knowledge

of the large, generalised model to our smaller, subject specific model.

In our approach, we use the FCNResNet101 network [24][14] pretrained on ImageNet to extract feature vectors for each pixel in an image, by taking the output of the first and second layers of the network (since the embeddings at these stages are less specialised to the ImageNet training data) and up sampling these to equal the resolution of the input image. We then use k-means clustering on the pixels' feature vectors, with a user determined k-value, to segment the image. Here, we can vary the segmentation granularity by controlling resampling of the image before feature extraction. Feature extraction at lower resolution allows us to extract larger scale information such as crystal phase domain shape, size, and location, each of which is useful in STM studies in its own right [36] [33]. An example of this is presented in Figure 3(f), where the stepped Si(001) surface in Figure 3(a) is segmented into two domains (dimer rows rotated by 90 degrees separated by atomic steps), identified by the purple and green regions. Feature extraction at higher resolution, as shown in 3(e), leads to more detailed segmentation with dimer rows and defects both being identified, but not yet clustered into meaningful classes. From this more granular segmentation, we can extract a binary map of the location of all defects. An example is shown in the yellow overlay of Figure 3(f). This process requires a graphics processing unit (GPU), taking up to five minutes for an image upsampled to 4160×4160 pixels on a Tesla T4 GPU. The slow computation and requirement for GPU access restricts the use of this method on the fly, during data acquisition, therefore the binary maps are used to train a U-Net for each new substrate, which can produce an output in seconds on a CPU. A faster, but less accurate, alternative is presented in Appendix 7.

3.3 Module 2: U-Net Binary Segmentation

Having produced labelled images for a particular substrate using module 1, we then train a U-Net [32], for use in module 2. This approach not only allows us to run our technique on a CPU but also allows for data augmentation to train a more robust network. We use a standard U-Net architecture with three down sampling layers, a bottleneck, and three up sampling layers. As with our FSL, we do not run a hyperparameter exploration. An example of the binary mapping,

via the U-Net, is shown in Figure 2(c), which maps images 2(a) and (b).

In training for our three substrate test cases, we use five scans each of 512×512 pixels resolution and $(100 \text{ nm})^2$, $(50 \text{ nm})^2$, and $(10 \text{ nm})^2$ in size for Si, Ge, and TiO_2 , respectively. We then apply data augmentation to deterministically add simulated experimental noise and STM tip artefacts to the scan data, and to increase the effective area of our scans by taking random crops of 64×64 pixels and rotating randomly by 0, 90, 180, or 270 degrees. Using crops in this way also teaches the network translational and rotational symmetry, which can be tailored to the symmetries of the surfaces studied. Finally, when making predictions about an unseen image, a method similar to Pielawski et al. is used [28]. We slice the image into overlapping crops of equal size to the random crops used in training, i.e. 64×64 pixels. The U-Net then segments each crop, and these are reassembled to give the final output. Overlapping the crops helps to reduce edge effects from the model [18].

3.4 Module 3: FSL Feature Classification

Few-shot learning is an ML technique to be used when labelled data is scarce. In this approach, the goal is to accurately classify unseen data using only a few examples of the data classes. FSL is generally described as an N-way K-shot classification problem. In each FSL problem, or episode, a support set, S , contains K labelled examples from N defined classes, and is used to infer the classification of an unseen query set, Q , which contains an equal distribution of samples to be classified into the N classes. An equal distribution is needed during training and testing to prevent over or under sampling and provide a fairer measure of accuracy but is not necessary during inference. At a higher level, as with supervised ML, there is still a training, test, and validation set: T_{tr} , T_{te} , and V , respectively. Crucially, since the goal is to train a network that can adapt well to new data, T_{tr} , T_{te} , and V cannot share any classes. In training, S and Q are generated by randomly sampling from T_{tr} , in testing from T_{te} , and in validating from V . In this paper, we focus on the metric-based approaches to FSL.

Figure 4 illustrates an episode of a metric based FSL algorithm. This consists of two stages: a) embedding and b) classification. After their definition, the support and query set are both embedded in a feature space using a neural network, $F(\text{image}, \vec{\theta})$,

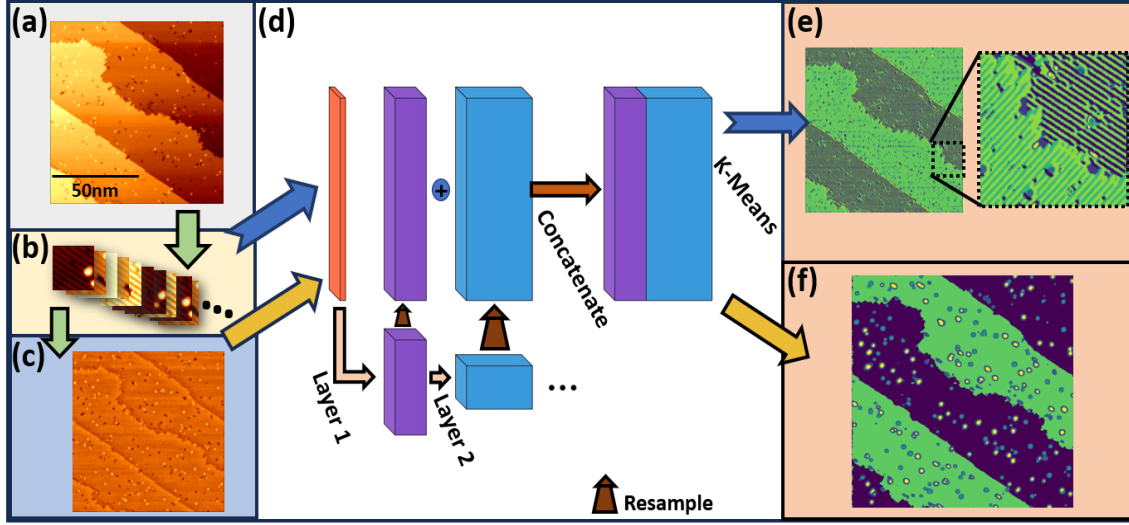


Figure 3: Overview of the unsupervised pipeline for STM image segmentation. (a) Original filled-state STM image of the Si(001):H:AsH₃ surface (100 nm × 100 nm, 512 × 512 pixels; acquired at -2 V, 50 pA). (b) The image is partitioned into 64 × 64 pixel patches with 32-pixel overlap. Each patch undergoes normalisation (min-max followed by z-score). (c) Reconstructed image after applying a sinusoidal window function to the patches in (b). This serves as one potential input pathway. (d) Feature extraction. The network incorporates resampling layers (indicated by 'Resample' arrows) to process features at different scales. Inputs are normalized (min-max, z-score) as is needed by the FCNResnet101 network. (b),(d),(e) Pathway 1: High-resolution segmentation. Patches from (b) are processed through the network, yielding 768-dimensional feature vectors per pixel. Subsequent k-means clustering (k=7) produces the final segmentation map shown in (e), with a zoomed-in region highlighting detail. (c),(d),(f) Pathway 2: Lower-resolution segmentation. The pre-processed image (c) is fed through the network. k-means clustering (k=5) is applied to the extracted features to generate the segmentation map (f).

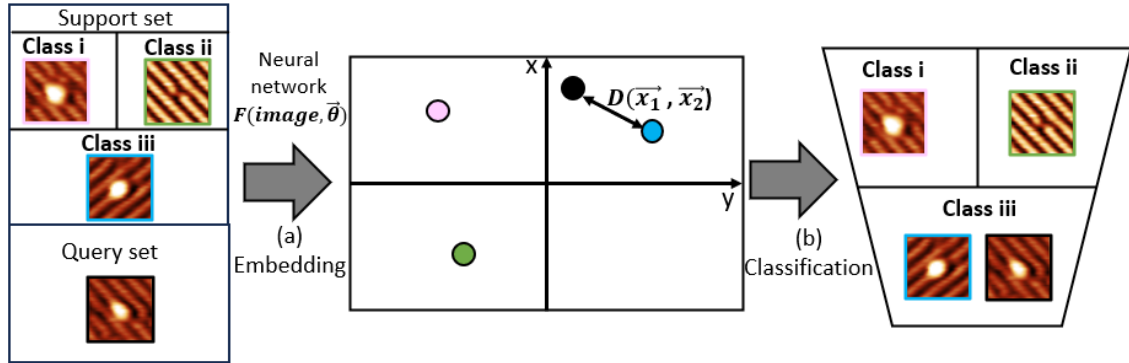


Figure 4: Illustration of a metric based approach to few-shot learning. $F(\text{image}, \vec{\theta})$ and $D(\vec{x}_i, \vec{x}_j)$ vary depending on the chosen approach. $\vec{\theta}$ are the weights of the neural network. The vector space is referred to as the latent space. Once images are (a) embedded in the vector space, they are (b) classified by determining the closest data point from the support set using $D(\vec{x}_i, \vec{x}_j)$ as the metric.

where $\vec{\theta}$ are the parameters of the network. Once the support and query set are embedded, the resulting feature vectors of the query set are compared to the feature vectors of the support set, using a specific distance metric, $D(\vec{x}_i, \vec{x}_j)$, where $\vec{x}_n \in \mathbb{R}^s$, $s \in \mathbb{N}$. The

query samples are then assigned to the classes of the support vectors that are closest within the vector space, according to metric D . In our example case of Si(001):H, the support and query sets consist of 2.5 nm × 2.5 nm crops of individual defects taken

from the STM image in Figure 1(a), where class (i) is double dangling bonds [5], class (ii) is siloxane [8], and class (iii) is single dangling bonds [8]. If these 2D STM crops are flattened, then they can also be viewed as 1D vectors. In essence, the aim is to train a network that can perform a dimensionality reduction on these vectors to remove redundancy while retaining any important information about the image crops, thus allowing for a better comparison between query and support set.

As illustrated in Figure 2(e) and (f), before passing all feature crops to the FSL module for classification, the user is first prompted to assess a subset of the data and define a support set of K examples of N feature classes, thus initializing the FSL module. All remaining crops are then fed directly to the FSL module as the query set. This support set can be redefined by the user, as required. Once all defects from an image have been classified by the FSL module, this result is combined with the U-Net binary segmentation to produce a fully segmented mask, as shown in Figure 2(h). This final output includes pixel coordinates of all defects.

As discussed below, we test the four different FSL algorithms summarized in Table 1: standard implementations of prototypical, matching, and simple-shot algorithms [35] [41] [43], and a modified version of the relation network [40] supporting a variable number of classes N (details provided in the Appendix 11.3). Due to its use of a second neural network for a distance metric, the relation network has a larger number of parameters and so requires extended training for accuracy to converge. This should be considered when comparing it to the other models.

To standardise our networks, and provide an even comparison, all network backbones use the same conv4 architecture that has been widely used throughout the ML community for accurate embeddings [13] [15]. The only augmentation used in training of the FSL networks is rotation of the defects at angles of 0, 90, 180, 270 degrees.

3.5 Workflow Benefits

The image recognition framework presented here is well-suited to STM data analysis because it relaxes the requirement for labelled data. This relaxation not only unburdens the user but also introduces a flexibility that can address the variability and the overwhelming detail inherent in atomic resolution STM

data. For example, the shape of the STM tip may change during measurement, having an influence on the appearance of features in the images. If a human user can recognize the features across tip changes, then the images can still be accurately segmented with our approach by adjusting the FSL support set, on the fly, in step (iv). This on-the-fly adjustment of the support set can also be used to tag anomalous features, marking them for exclusion from final statistics. This is an advance on the supervised learning of Rashidi et.al. [29] where no provision is made for anomalies, meaning they are incorrectly classified as one of the predefined classes. While the unsupervised clustering technique of Ziatdinov et al. [47] can deal with anomalies, no accuracies are provided since the approach is unsupervised. Our workflow provides opportunity for the user to exclude anomalous features, allowing the FSL network to classify only the repeating defects of interest. Furthermore, while the workflow presented here is a specific implementation of our image recognition framework, our modular code is flexible, permitting alternative implementations. For example, the FSL network might be used to perform a dimensionality reduction of the data, followed by unsupervised clustering on these latent space vectors, as done by Ziatdinov et al.

4 Results & Discussion

We now assess the workflow when used to segment STM images from each of our three test cases: Si, Ge, and TiO_2 . For segmentation tasks, accuracies alone can be misleading. We therefore provide a second metric: the dice scores (DS), where $DS = \frac{A \cap B}{|A| + |B|}$, and A and B are any two sets. We provide both the DS for the lattice defects alone (i.e. the class of immediate interest in our test cases), and also the total DS for both the background lattice *plus* defects, thus allowing direct comparison with the DSs provided by Rashidi et al. [29].

4.1 U-Net Segmentation

Table 2 summarizes the U-Net performance on the three test cases. Here we achieve accuracies that are all above 90%, with the U-Net performing best on the germanium and worst on the titania. With regards to the dice score metric, we find the network also performs best on the germanium, with a $DS = 0.99$.

FSL network	Training type	Training length	Distance metric
Protoypical [35]	Episodic	2000 episodes	Euclidean
Matching [41]	Episodic	2000 episodes	Cosine
Relation [40]	Episodic	5000 episodes	Multi-layer perceptron (MLP)
Simple shot [43]	Normal	20 epochs	Euclidean

Table 1: Different FSL networks used. The training length was chosen such that the test accuracy converged. The relation network required more episodes since it has more weights to optimise than the other networks.

Within our workflow, the FSL network classifies the defects, therefore, the U-Net need only provide the FSL module with an accurate estimate of the defects and not the background lattice. It is the DS for the defects alone then, that is most important to gauge the effectiveness of the U-Nets. A high accuracy but low DS, as in the case of the silicon (96.3% and 0.64 respectively), suggests the network struggles with boundary precision. The network likely struggles more with boundaries of the small surface defects in the case of the silicon data, since this data has the highest nm to pixel ratio.

As noted, Rashidi et al. provide an overall dice score including defects plus background and report a total DS = 0.86 for their supervised segmentation of the Si(001):H surface [29]. This is significantly lower than our result of total DS = 0.96, but it should be remembered that their network assessed seven classes. This is inherently harder than the two classes used in our case but also comes at the cost of requiring five times more labelled data at this segmentation stage.

Surface	Val acc	Dice score (defects)	Dice score (total)
Si(001) /Si(001):H	96.3%	0.64	0.96
Ge(001)	99.0%	0.87	0.99
TiO ₂ (110)	90.1%	0.88	0.96

Table 2: Validation accuracies and dice scores of the U-Net for the three different surfaces.

4.2 FSL Classifications

Alongside the four FSL networks explored, we also include a k-nearest neighbour (kNN) classification on the bare pixels. This provides a baseline for a comparison of each of the embedding methods. Mean shift clustering was also investigated but found to be

very sensitive to the bandwidth (i.e. the radius used to calculate the mean in each iteration step), thus proving too difficult to automate.

To assess the suitability of our FSL module for analysis of STM data corresponding to a known substrate exposed to an unknown adsorbate, we first test the FSL algorithms when classifying unseen features in the silicon data after having been trained on a subset of known features on this same surface. Although the Si(001):H surface contains many well understood defect types [8], the majority of these features are relatively rare and not easily included in the training data. By grouping the bare Si(001), Si(001):H and Si(001):H:AsH₃ surfaces together, we provide sufficient, regularly occurring defects within the dataset to allow for training, validation, and test data that do not share classes. In this way the network is trained on the known substrate, silicon, and tested on a set of unseen features that are a stand-in for a new unknown adsorbate.

In contrast, the germanium and titania cases are introduced as examples where both substrate and adsorbate are unknown. We test the FSL algorithms on the Ge(001):AsH₃ after having been trained on only the silicon and titania data and on the TiO₂(110) after having only been trained on silicon and germanium data. That is, for the germanium and titania examples, the training and validation datasets do not contain any germanium and titania data respectively, but the test sets do. The class splits for the training, testing, and validation sets in all of the test cases are detailed in Table 3. Note, in the case of kNN the training data appears identical to the test data due to the terminology for kNN being different to that of the FSL algorithms, which all contain neural networks. Full details of every feature type used in training, test and validation are provided in Appendix 11.1.

Alongside the training and validation details of our test cases, Table 3 also presents accuracies for 1- and

Si(001):H:AsH ₃ (test set of classes 5-8)			
Model	Training & validation data	Acc (4-way, 1-shot)	Acc (4-way, 3-shot)
Prototypical	Classes 1-4, 9-15 and their inverses	93.3 ± 0.4 %	97.6 ± 0.1 %
Matching	Classes 1-4, 9-15 and their inverses	93.3 ± 0.3 %	96.5 ± 0.5%
Relation	Classes 1-4, 9-15 and their inverses	84.6 ± 0.4%	81.2 ± 0.2%
Simple shot (conv4)	Classes 1-4, 9-15 and their inverses	92.9 ± 0.1%	93.6 ± 0.1%
Simple shot (ResNet18)	ImageNet	66.9 ± 0.3%	91.2 ± 0.1%
kNN (k=1) on bare pixels	Classes 5-8	76.6 ± 0.2%	91.4 ± 0.1%
Ge(001):AsH ₃ (test set of classes 9-13)			
Model	Training & validation data	Acc (4-way, 1-shot)	Acc (4-way, 3-shot)
Prototypical	Classes 1-8, 14-15 and their inverses	61.3 ± 0.2%	68.5 ± 0.1 %
Matching	Classes 1-8, 14-15 and their inverses	61.6 ± 0.2 %	66.5 ± 0.1%
Relation	Classes 1-8, 14-15 and their inverses	25.1 ± 0.1%	62.6 ± 0.1%
Simple shot (conv4)	Classes 1-8, 14-15	48.2 ± 0.1%	51.0 ± 0.1%
Simple shot (ResNet18)	ImageNet	43.0 ± 0.2%	68.3 ± 0.2%
kNN (k=1) on bare pixels	Classes 9-13	46.6 ± 0.2%	62.7 ± 0.1%
TiO ₂ (110) (test set of classes 14-15)			
Model	Training & validation data	Acc (2-way, 1-shot)	Acc (2-way, 3-shot)
Prototypical	Classes 1-13 and their inverses	70.3 ± 0.3 %	74.1 ± 0.2%
Matching	Classes 1-8	61.6 ± 0.2%	63.4 ± 0.2%
Relation	Classes 1-8	30.9 ± 0.3%	55.7 ± 0.3%
Simple shot (conv4)	Classes 1-8	54.5 ± 0.2%	57.5 ± 0.3%
Simple shot (ResNet18)	ImageNet	65.0 ± 0.2%	76.3 ± 0.2 %
kNN (k=1) on bare pixels	Classes 14-15	57.4 ± 0.3%	71.5 ± 0.3%

Table 3: Accuracies for the different FSL algorithms on the silicon, germanium, and titanium dioxide datasets. Classes 1-8 are from Si(001) and Si(001):H:AsH₃, classes 9-13 are from Ge(001):AsH₃, and classes 14-15 are from TiO₂(110). Results shown here are a subset of all results obtained and are the best outcomes for each algorithm-dataset-substrate triplet. Results from the best performing algorithm for each surface are highlighted in bold. More details about the classes be seen in Appendix 11.1. More details on the inverse classes in the ablation study are presented in section 4.3. Conv4 and ResNet18 refer to the backbones used for the simple shot network. Results are accuracies averaged over 100 episodes and with 95% confidence interval, with query sets containing 15 images per class.

3-shot FSL classifications performed by each of the FSL algorithms. Comparing the results from each embedding across the different test cases, we find the prototypical and matching algorithms tend to produce the highest accuracy. Even with as little as one labelled image of the features, these algorithms can achieve a 93% accuracy when applied to the silicon data. Next best is the simple shot model, which we find performs much better when using conv4 instead of ResNet18 for the embedding. We also note that computation was much slower when using Resnet18, due to the large size of this network. Finally, the relation network performs drastically worse than all other networks, specifically in the 1-shot classification. The distance function, $D(\vec{x}_i, \vec{x}_j)$, of the relation network is a second neural network, whereas the others use fixed distance functions, therefore, it is likely that low accuracies of the relation network are due in part to over fitting to the training data. Neverthe-

less, the embeddings of nearly all the FSL networks examined offer an increase in accuracy compared to the kNN baseline, without further training. This is the case even in the most challenging example of the Ge(001):AsH₃ data where the accuracies are considerably lower due to subtler differences between detected features. The results from the best performing FSL algorithm for each test case are presented in Figure 5, here a segmented and fully classified image is presented for each studied surface.

4.3 Improving Accuracies: Ablation Study

Finally, is it possible to improve on the reported accuracies without resorting to labelling more data? The classification accuracies of the FSL networks depend on how well they can embed the images into the latent vector space. Intuition would suggest that a larger variety of defect classes seen during training would

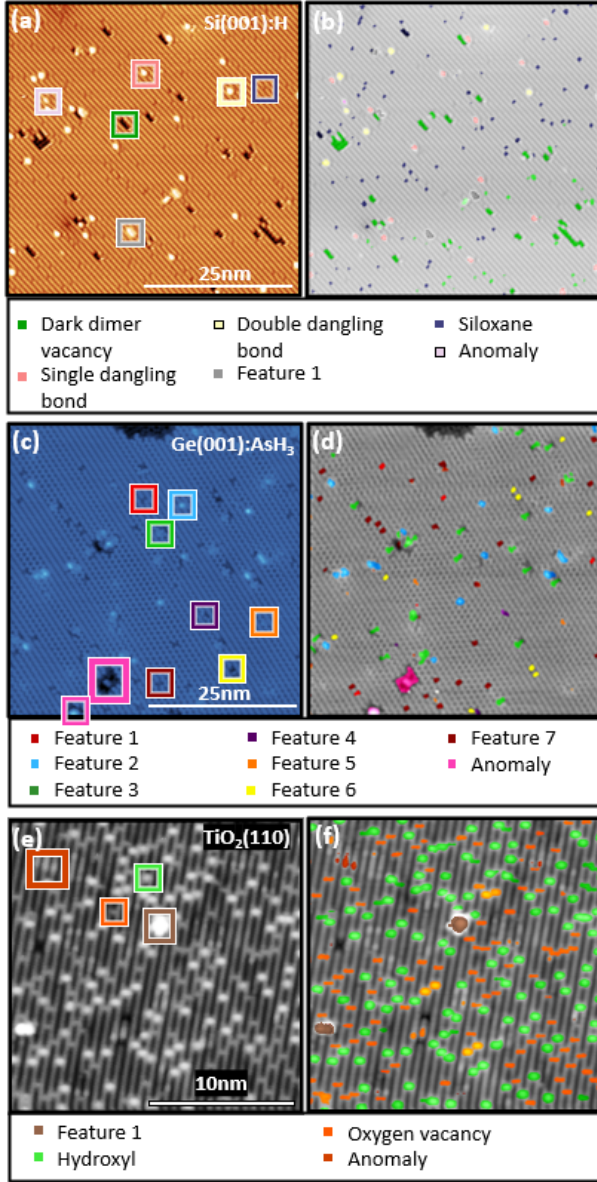


Figure 5: Final image segmentation plus feature classification on the three substrates: (a) Si(001) (b) Ge(001):AsH₃ (c) TiO₂(110). The colour coded squares around the features are the ones that were given as examples to the few-shot learning algorithm. In each case we use the best performing algorithm for that substrate from Table 3, where the corresponding accuracies can be found.

result in higher quality embedding. To test this, we supplement the datasets with artificial defects, formed by inverting the pixel values of real defect images to produce negative images, and in effect, new defect types. In this way, we show that the data supports our intuition; the accuracies of our models increase

when we increase the number of classes in $\mathcal{C}(T_r)$. For example, when using the Ge(001):AsH₃ data as our validation set, we double the size of our training and test set from classes 1-8 to classes 1-8 plus all inverses. As a result, the prototypical network accuracy increases by 6% in the 1-shot case, while the matching network improves by almost 16%. This initial success is promising and establishes a path to further increase the effectiveness of our STM segmentation approach without increasing the demand on manual data labelling. In the appendix 11.4 we provide a table with further exploration of accuracy improvements through artificial dataset size increases.

5 Conclusion

We have developed a machine learning image recognition methodology that is catered specifically for segmentation of atomically resolved STM images of unseen adsorbates and substrates. Our approach offers enhanced flexibility compared to previous studies while demanding significantly less labelled training data, all while achieving 1-shot accuracies of up to 93%, 62%, and 70% in our test cases of silicon, germanium, and titania respectively, and even higher in the 3-shot case. While a 93% accuracy rate would generally be sufficient for drawing definitive conclusions about the surface chemistry of the substrate and adsorbate, 62% would not be. However, the adaptability of the proposed method makes it a valuable tool for real-time image segmentation and labelling in a laboratory setting, enabling users to rapidly gain insight into ongoing processes, even with accuracies of 70%.

The bottleneck to this approach is the need for new segmented labelled data when working with a new surface. We have therefore introduced a pipeline to ease the segmentation by implementing unsupervised methods in a training data labelling module. Next, a coarse segmentation module discerns lattice irregularities, demonstrating robust performance even with as few as 4 or 5 scans. Finally, a classification module uses FSL networks to embed the surface features into a latent space before classifying them. The FSL networks tested here exhibit optimal results with data from the same surface used for training, but in all test cases, including unseen surfaces, these networks can elevate accuracies beyond traditional clustering methods on raw pixels, even when the application of

traditional kNN shows accuracies as high as 75% in the 1-shot case. Furthermore, we have also presented a novel architecture for the relation network that allows for a variable number of classes without loss of accuracy.

Finally, rather than develop optimised networks for our data, in this study we have used standard architectures shown to work well in previous studies. This approach has simplified the initial assessment of FSL techniques for STM image segmentation, but it also leaves room for improvement. Having clearly established the suitability of FSL for STM image recognition, improvements should now be realised by implementing a hyperparameter exploration. In this way, progress can be continued towards an efficient and material-agnostic, automatic segmentation of STM images with minimal labelled data requirements.

6 Experimental

The three substrate systems (Si(001):H:AsH₃, Ge(001):AsH₃, TiO₂) are prepared as detailed in references [38], [17], and [45] respectively. The silicon systems were measured using an Omicron variable temperature STM, while the germanium was measured using an Omicron low temperature STM. Silicon and germanium were all measured at room temperature. The titania with an Omicron low temperature STM at 78 K. Training of the U-Net was carried out over 60 epochs, with a batch size of 500, a learning rate of 0.01 that decays by 0.1 every 15 epochs, and a binary cross entropy loss. Training of the FSL networks were carried out with a learning rate of 0.001 (their training lengths were given in Table 1) with a cross entropy loss. Simple shot used batch sizes of 32, while the rest were trained using episodes.

7 Acknowledgments

This project was financially supported by the Engineering and Physical Sciences Research Council (EPSRC) [grant numbers EP/V027700/1, and EP/W000520/1], Innovate UK [grant number UKRI/75574], and ERC AdvG ENERGYSURF. N.L.K., M.T and E.V.S.H were partly supported by the EPSRC Centre for Doctoral Training in Advanced Characterisation of Materials [grant number

EP/L015277/1] and Nanolayers Research Computing. We thank Emily V.S Hofmann for providing us with the Ge(001):AsH₃ data in this study.

8 Conflict of Interest

The authors declare no conflict of interest.

9 Data Availability Statement

The data that support the findings of this study are openly available at <https://doi.org/10.5281/zenodo.15525935>.

10 Code Availability

The code and models trained can be found on github at https://github.com/nickkolev97/FSL_STM.

References

- [1] Sarah Akers, Elizabeth Kautz, Andrea Trevino-Gavito, Matthew Olszta, Bethany E. Matthews, Le Wang, Yingge Du, and Steven R. Spurgeon. Rapid and flexible segmentation of electron microscopy data using few-shot machine learning. *npj Computational Materials*, 7(1):187, 2021.
- [2] Anwai Archit, Sushmita Nair, Nabeel Khalid, Paul Hilt, Vikas Rajashekar, Marei Freitag, Sagnik Gupta, Andreas Dengel, Sheraz Ahmed, and Constantin Pape. Segment anything for microscopy. *bioRxiv*, 2023.
- [3] Oier Bikondoa, Chi L Pang, Roslinda Ithnin, Christopher A Muryn, Hiroshi Onishi, and Geoff Thornton. Direct visualization of defect-mediated dissociation of water on tio2 (110). *Nature materials*, 5(3):189–192, 2006.
- [4] G. Binnig, H. Rohrer, Ch. Gerber, and E. Weibel. 7×7 reconstruction on si(111) resolved in real space. *Phys. Rev. Lett.*, 50:120–123, Jan 1983.
- [5] D. R. Bowler, J. H. G. Owen, K. Miki, and G. A. D. Briggs. Diffusion of paired hydrogen on si(001). *Phys. Rev. B*, 57:8790–8793, Apr 1998.

- [6] S. K. Broome, M. A. and Gorman, M. G. House, S. J. Hile, J. G. Keizer, D. Keith, Hill C. D., T. F. Watson, W. J. Baker, L. C. L. Hollenberg, and M. Y. Simmons. Two-electron spin correlations in precision placed donors in silicon. *Nature Communications*, 9, March 2018.
- [7] K. Choudhary, Camp C. Kevin F., Kalinin Sergei V., R. Vasudevan, M. Ziatdinov, and F. Tavazza. Computational scanning tunneling microscope image database. *Scientific Data*, 2021.
- [8] Jeremiah Croshaw, Thomas Dienel, Taleana Huff, and Robert Wolkow. Atomic defect classification of the h-si(100) surface through multi-mode scanning probe microscopy. *Beilstein Journal of Nanotechnology*, 11:1346–1360, sep 2020.
- [9] Ulrike Diebold. The surface science of titanium dioxide. *Surface Science Reports*, 48(5):53–229, 2003.
- [10] O. Gordon, P. D’Hondt, L. Knijff, S. E. Freeney, F. Junqueira, P. Moriarty, and I. Swart. Scanning tunneling state recognition with multi-class neural network ensembles. *Review of Scientific Instruments*, 90(10):103704, 10 2019.
- [11] Oliver M Gordon, Filipe LQ Junqueira, and Philip J Moriarty. Embedding human heuristics in machine-learning-enabled probe microscopy. *Machine Learning: Science and Technology*, 1(1):015001, 2020.
- [12] Georg Gramse, Alexander Kölker, Tomáš Škerek, Taylor JZ Stock, Gabriel Aeppli, Ferry Kienberger, Andreas Fuhrer, and Neil J Curson. Nanoscale imaging of mobile carriers and trapped charges in delta doped silicon p–n junctions. *Nature Electronics*, 3(9):531–538, 2020.
- [13] Yueming Hao, Xu Zhao, Bin Bao, David Berard, Will Constable, Adnan Aziz, and Xu Liu. Torchbench: Benchmarking pytorch with high api surface coverage. *arXiv e-prints*, pages arXiv–2304, 2023.
- [14] Kaiming He, Xiangyu Zhang, Shaoqing Ren, and Jian Sun. Deep residual learning for image recognition. *CoRR*, abs/1512.03385, 2015.
- [15] Kaiming He, Xiangyu Zhang, Shaoqing Ren, and Jian Sun. Deep residual learning for image recognition. *CoRR*, abs/1512.03385, 2015.
- [16] Calum Heggan, Sam Budgett, Timothy Hospedales, and Mehrdad Yaghoobi. Metaaudio: A few-shot audio classification benchmark. In *International Conference on Artificial Neural Networks*, pages 219–230. Springer, 2022.
- [17] Emily V. S. Hofmann, Taylor J. Z. Stock, Oliver Warschkow, Rebecca Conybeare, Neil J. Curson, and Steven R. Schofield. Room temperature incorporation of arsenic atoms into the germanium (001) surface. *Angewandte Chemie International Edition*, 62(7):e202213982, 2023.
- [18] Carlo Innamorati, Tobias Ritschel, Tim Weyrich, and Niloy J. Mitra. Learning on the edge: Explicit boundary handling in cnns. *CoRR*, abs/1805.03106, 2018.
- [19] Frédéric Joucken, John L. Davenport, Zhehao Ge, Eberth A. Quezada-Lopez, Takashi Taniguchi, Kenji Watanabe, Jairo Velasco, Jérôme Lagoute, and Robert A. Kaindl. Denoising scanning tunneling microscopy images of graphene with supervised machine learning. *Phys. Rev. Mater.*, 6:123802, Dec 2022.
- [20] Kevin Kaufmann, Hobson Lane, Xiao Liu, and Kenneth S Vecchio. Efficient few-shot machine learning for classification of ebsd patterns. *Scientific reports*, 11(1):8172, 2021.
- [21] Abid Khan, Chia-Hao Lee, Pinshane Y. Huang, and Bryan K. Clark. Leveraging generative adversarial networks to create realistic scanning transmission electron microscopy images. *npj Computational Materials*, 9(1), may 2023.
- [22] A. Krull, P. Hirsch, C. Rother, A. Schiffrin, and Krull C. Artificial-intelligence-driven scanning probe microscopy. *Nature*, Mar 2020.
- [23] Diyang Liu, Xunzhang Gao, and Qinmu Shen. Prototypical network for radar image recognition with few samples. *Journal of Physics: Conference Series*, 1634(1):012116, sep 2020.

- [24] Jonathan Long, Evan Shelhamer, and Trevor Darrell. Fully convolutional networks for semantic segmentation. *CoRR*, abs/1411.4038, 2014.
- [25] JW Lyding, T-C Shen, JS Hubacek, JR Tucker, and GC Abeln. Nanoscale patterning and oxidation of h-passivated si (100)- 2×1 surfaces with an ultrahigh vacuum scanning tunneling microscope. *Applied physics letters*, 64(15):2010–2012, 1994.
- [26] Kamalesh Palanisamy, Yu-Wei Chao, Xinya Du, Yu Xiang, et al. Proto-clip: Vision-language prototypical network for few-shot learning. In *2024 IEEE/RSJ International Conference on Intelligent Robots and Systems (IROS)*, pages 2594–2601. IEEE, 2024.
- [27] Chi Lun Pang, Robert Lindsay, and Geoff Thornton. Structure of clean and adsorbate-covered single-crystal rutile tio₂ surfaces. *Chemical reviews*, 113(6):3887–3948, 2013.
- [28] Nicolas Pielawski and Carolina Wählby. Introducing hann windows for reducing edge-effects in patch-based image segmentation. *PLOS ONE*, 15(3):e0229839, March 2020.
- [29] Mohammad Rashidi, Jeremiah Croshaw, Kieran Mastel, Marcus Tamura, Hedieh Hosseinzadeh, and Robert A Wolkow. Deep learning-guided surface characterization for autonomous hydrogen lithography. *Machine Learning: Science and Technology*, 1(2):025001, mar 2020.
- [30] Mohammad Rashidi and Robert A Wolkow. Autonomous scanning probe microscopy in situ tip conditioning through machine learning. *ACS nano*, 12(6):5185–5189, 2018.
- [31] Marcel Reutzelt, Gerson Mente, Peter Stromberger, Ulrich Koert, Michael Dürr, and Ulrich Höfer. Dissociative adsorption of diethyl ether on si(001) studied by means of scanning tunneling microscopy and photoelectron spectroscopy. *The Journal of Physical Chemistry C*, 119, March 2015.
- [32] Olaf Ronneberger, Philipp Fischer, and Thomas Brox. U-net: Convolutional networks for biomedical image segmentation. In *Medical image computing and computer-assisted intervention–MICCAI 2015: 18th international conference, Munich, Germany, October 5-9, 2015, proceedings, part III 18*, pages 234–241. Springer, 2015.
- [33] Hyungjoon Shim and Geunseop Lee. True first-order surface phase transition without nanoscale phase separation. *ACS Nano*, 17, Jul 2023.
- [34] Tomáš Škřeň, Sigrun A Köster, Bastien Douhard, Claudia Fleischmann, and Andreas Fuhrer. Bipolar device fabrication using a scanning tunnelling microscope. *Nature Electronics*, 3(9):524–530, 2020.
- [35] Jake Snell, Kevin Swersky, and Richard Zemel. Prototypical networks for few-shot learning. *Advances in neural information processing systems*, 30, 2017.
- [36] Sun Kyu Song and Han Woong Yeom. Atomistic origin of metal versus charge-density-wave phase separation in indium atomic wires on si(111). *Phys. Rev. B*, 104:035420, Jul 2021.
- [37] Yisheng Song, Ting Wang, Puyu Cai, Subrota K Mondal, and Jyoti Prakash Sahoo. A comprehensive survey of few-shot learning: Evolution, applications, challenges, and opportunities. *ACM Computing Surveys*, 55(13s), 2023.
- [38] Taylor JZ Stock, Oliver Warschkow, Procopios C Constantinou, David R Bowler, Steven R Schofield, and Neil J Curson. Single-atom control of arsenic incorporation in silicon for high-yield artificial lattice fabrication. *Advanced Materials*, 36(24):2312282, 2024.
- [39] Joshua Stuckner, Bryan Harder, and Timothy M Smith. Microstructure segmentation with deep learning encoders pre-trained on a large microscopy dataset. *npj Computational Materials*, 8(1):200, 2022.
- [40] Flood Sung, Yongxin Yang, Li Zhang, Tao Xiang, Philip HS Torr, and Timothy M Hospedales. Learning to compare: Relation network for few-shot learning. In *Proceedings of the IEEE conference on computer vision and pattern recognition*, pages 1199–1208, 2018.
- [41] Oriol Vinyals, Charles Blundell, Timothy Lillicrap, Daan Wierstra, et al. Matching networks

for one shot learning. *Advances in neural information processing systems*, 29, 2016.

- [42] Xiqiao Wang, Jonathan Wyrick, Ranjit V. Kashid, Pradeep Namboodiri, Andrew Schmucker, Scott W. and Murphy, M. D. Stewart, and Richard M. Silver. Atomic-scale control of tunneling in donor-based devices. *Communications Physics*, 3, May 2020.
- [43] Yan Wang, Wei-Lun Chao, Kilian Q Weinberger, and Laurens van der Maaten. Simpleshot: Revisiting nearest-neighbor classification for few-shot learning. *arXiv e-prints*, pages arXiv–1911, 2019.
- [44] O. Warschkow, N. J. Curson, S. R. Schofield, N. A. Marks, H. F. Wilson, M. W. Radny, P. V. Smith, T. C. G. Reusch, D. R. McKenzie, and M. Y. Simmons. Reaction paths of phosphine dissociation on silicon (001). *The Journal of Chemical Physics*, 144(1):014705, 01 2016.
- [45] Oscar Bentley Jerdmyr Williams, Khabiboulakh Katsiev, Byeongjin Baek, George Harrison, Geoff Thornton, and Hicham Idriss. Direct visualization of a gold nanoparticle electron trapping effect. *Journal of the American Chemical Society*, 144(2):1034–1044, 2022.
- [46] Zhirui Zhang, Zhiqiang Zou, Nan Li, and Yanli Chen. Classifying galaxy morphologies with few-shot learning. *Research in Astronomy and Astrophysics*, 22(5):055002, 2022.
- [47] Maxim Ziatdinov, Udi Fuchs, James HG Owen, John N Randall, and Sergei V Kalinin. Robust multi-scale multi-feature deep learning for atomic and defect identification in scanning tunneling microscopy on h-si (100) 2x1 surface. *arXiv e-prints*, pages arXiv–2002, 2020.
- [48] Maxim Ziatdinov, Ayana Ghosh, Chun Yin Wong, and Sergei V. Kalinin. Atomai framework for deep learning analysis of image and spectroscopy data in electron and scanning probe microscopy. *Nature Machine Intelligence*, 4(12):1101–1112, December 2022.

11 Appendix

11.1 Datasets

The full dataset used for this work includes data from the 4 different surfaces (Si(001), Si(001):H:AsH₃, Ge:AsH₃, and TiO₂) and contains two types of labelled data, as detailed in table 4. These are: (1) fully segmented scans which have any defect in the lattice highlighted (except for step edges), and (2) scans with pixel coordinates and labels for the defects present on their surface. Due to the nature of STM, if we contrast inverse an image of a defect (i.e. turn a depression into a protrusion and vice-versa), we can produce a new 'defect'. This 'defect', is of course not seen in the STM data, but it can be used for training and validating our models. We show in section 4.3 that this method of increasing our dataset increases the accuracy of our model. Although our model works with filled and empty state images, the TiO₂(110) dataset was only available as empty state images. In this case, we repeat the empty state images to make a tensor of the same shape, allowing us to use the same networks.

The different defects used for training of the FSL networks are shown in Figure 6. Features h1 and h2 were very rare in the experimental data. As a result, during training, testing, and validating we augmented those crops using rotations and reflections thus producing a sufficient number of examples to allow a 4-way, 1-shot or 4-way, 3-shot episode. This is not good practice usually since the network will see augmented versions of the same data in both training and testing leading to less resilient results. However, doing so was necessary to allow us to use this data.

Dataset	Crops (C) or fully segmented (FS)?	Si(001):H & Si(001):H:AsH ₃	Ge:AsH ₃ (001)	TiO ₂ (110)
5 × 100 nm ² scans at 512 × 512 pixels	FS	✓	×	×
5 × 50 nm ² scans at 512 × 512 pixels	FS	×	✓	×
4 × 10 nm ² scans at 512 × 512 pixels	FS	×	×	✓
1085 crops 11 × 11 pixels pixels	C	✓	×	×
198 crops 22 × 22 pixels pixels	C	×	✓	×
121 crops 61 × 61 pixels pixels	C	×	×	✓

Table 4: Description of dataset structures and data types for all data used in this study.



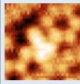
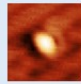

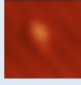

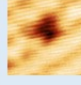
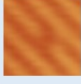
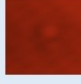
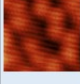

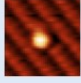


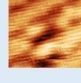
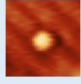
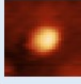

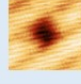

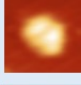
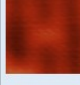

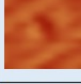


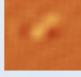
Defect name & number	Surface?	Number of data points	Filled state	Empty state	Defect name & number	Surface?	Number of data points	Filled state	Empty state
Single dangling bond (1)	Si(001)-H	349			t1 (9)	Ge(001):AsH ₃	114		
C defect (2)	Si(001)	89			g1 (10)	Ge(001):AsH ₃	24		
Siloxane (3)	Si(001)-H	186			h1 (11)	Ge(001):AsH ₃	2		
AsA (4)	Si(001)-H + AsH ₃	94			h2 (12)	Ge(001):AsH ₃	10		
AsB (5)	Si(001)-H + AsH ₃	29			m1 (13)	Ge(001):AsH ₃	48		
Double dangling bond (6)	Si(001)-H	216			Oxygen vacancy (14)	TiO ₂ (110)	71		
Single missing dimer (7)	Si(001)	31			Hydroxyl (15)	TiO ₂ (110)	50		
Single dihydride (8)	Si(001)-H	91							

Figure 6: Crops of the different features used to train and evaluate our networks.

11.2 A quicker auto-labelling procedure

Figure 7 details an automated unsupervised labelling technique that can pick out the defects without need for a GPU. Although it can pick out the defects, but it can not be tuned to segment phase structures, so is less flexible than the method presented in section 3.2. an automated unsupervised labelling technique can segment the dimers to some degree, if k-means clustering is used on Figure 7(c) instead of just thresholding, but not with the same accuracy as in section 3.2, especially at the step edges. The main difference between these two approaches, is that the method illustrated in Figure 7 does not perform any feature extraction using a pretrained network. Here, the k-means clustering or thresholding is performed on the pixels rather than on feature vectors.

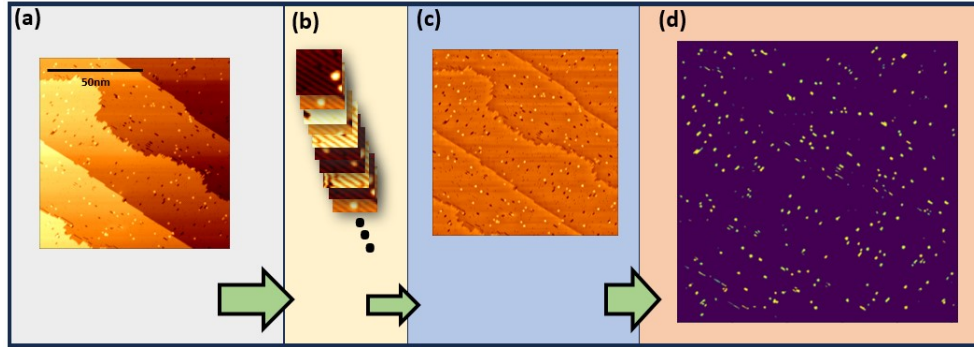


Figure 7: Less computationally heavy procedure for unsupervised labelling. The procedure from (a) to (c) is the same as that in Figure 3. From (c) to (d), we extract anything that is more or less than 3 standard deviations from the mean.

11.3 Relation Network Modification

We introduce a slight modification to the relation network. In the original relation network paper [40], the query feature vector is concatenated with each support vector and the full tensor of shape $(N, K, 2 \times d)$ is forwarded through the relation module at once, as shown in figure 8 (a) (where d is the dimension of the feature space). This architecture does not allow us to change N . However, the number of species on a surface recorded by an STM will vary between experiments, meaning a variable N . The proposed modified architecture, finds the relation scores in a pairwise fashion for each query and support vector separately. These are then combined to give a prediction. To the best of our knowledge, there is no literature that shows a relation network that has previously been used in this way to allow for a variable N . Since the relation network’s distance metric is a second neural network, called the relation module, it has more parameters than the other networks investigated. The original has $2NKdm_L \prod_{n=1}^{L-1} m_L + \sum_{n=1}^{L-1} m_i$ more, while the siamese relation network has $4Kdm_L \prod_{n=1}^{L-1} m_L + \sum_{n=1}^{L-1} m_i$ more (where m_i are the number of nodes in each hidden layer of the relation module, and L is the number of hidden layers).

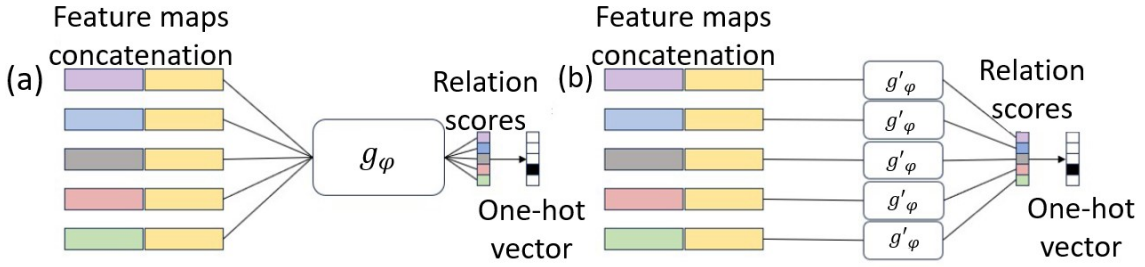


Figure 8: (a) The relation module from the original relation network paper with a neural network metric g_ϕ [40]. The non-yellow blocks are the feature vectors of the query vectors. The support vector’s feature vector is represented by the yellow blocks. (b) The relation module used in this work. g'_ϕ takes a single feature map concatenation at a time and outputs a relation score. This allows for a variable number of classes, N , and shots, K . The colour coding of the blocks corresponds to the same vectors as in (a).

11.4 Ablation study continued

Table 5 illustrates the effects of training the FSL networks using a larger variety of data.

Model	$\mathcal{C}(T_{tr}) \& \mathcal{C}(T_{te})$	$\mathcal{C}(V)$	Acc (4-way, 1-shot)	Acc (4-way, 3-shot)
Prototypical	defects 1-8	defects 9-13	$55.7 \pm 0.2\%$	$65.3 \pm 0.2\%$
Prototypical	defects 1-8 and their inverses	defects 9-13	$61.3 \pm 0.2\%$	$68.5 \pm 0.1\%$
Matching	defects 1-8	defects 9-13	$45.5 \pm 0.2\%$	$54.9 \pm 0.2\%$
Matching	defects 1-8 and their inverses	defects 9-13	$61.6 \pm 0.2\%$	$66.5 \pm 0.1\%$
Relation	defects 1-8	defects 9-13	$24.8 \pm 0.2\%$	$41.0 \pm 0.2\%$
Relation	defects 1-8 and their inverses	defects 9-13	$25.7 \pm 0.1\%$	$62.6 \pm 0.1\%$
Simple shot (conv4)	defects 1-8	defects 9-13	$48.2 \pm 0.1\%$	$51.0 \pm 0.1\%$
Simple shot (ResNet18)	ImageNet	defects 9-13	$43.0 \pm 0.2\%$	$68.3 \pm 0.2\%$
kNN (k=1) on bare pixels	defects 9-13	defects 9-13	$46.6 \pm 0.2\%$	$62.7 \pm 0.1\%$
kNN (k=3) on bare pixels	defects 9-13	defects 9-13	$46.6 \pm 0.2\%$	$58.9 \pm 0.2\%$
Model	$\mathcal{C}(T_{tr}) \& \mathcal{C}(T_{te})$	$\mathcal{C}(V)$	Acc (2-way, 1-shot)	Acc (2-way, 3-shot)
Prototypical	defects 1-8	defects 14-15	$69.2 \pm 0.2\%$	$66.4 \pm 0.2\%$
Prototypical	defects 1-13 and their inverses	defects 14-15	$70.0 \pm 0.3\%$	$74.1 \pm 0.2\%$
Matching	defects 1-8	defects 14-15	$61.6 \pm 0.2\%$	$63.4 \pm 0.2\%$
Matching	defects 1-13 and their inverses	defects 14-15	$52.5 \pm 0.3\%$	$60.3 \pm 0.2\%$
Relation	defects 1-8	defects 14-15	$30.9 \pm 0.3\%$	$55.1 \pm 0.3\%$
Simple shot (conv4)	defects 1-8	defects 14-15	$54.5 \pm 0.2\%$	$57.5 \pm 0.3\%$
Simple shot (ResNet18)	ImageNet	defects 14-15	$65.3 \pm 0.02\%$	$76.3 \pm 0.2\%$
kNN (k=1) on bare pixels	defects 14-15	defects 14-15	$57.4 \pm 0.3\%$	$71.5 \pm 0.3\%$
kNN (k=3) on bare pixels	defects 14-15	defects 14-15	$67.0 \pm 0.4\%$	N/A

Table 5: Classification accuracies on different subsets of our full dataset (MLSTM) data. Results are accuracies averaged over 100 episodes and with 95% confidence interval. Accuracies listed here are assuming that each class appears an equal number of times to give a fair representation of accuracy.

11.5 Application of unsupervised segmentation to STEM data

The unsupervised labelling method described in section 3 may also be useful for other microscopy techniques. In Figure 9 we display a comparison of the output from our method to that of reference [1], which describes course segmentation of STEM data using a prototypical network. Our technique can segment down to the pixel level, since we extract features for each pixel rather than a patch. Our approach allows users to vary the level of detail they desire, from phase separation to atomic level segmentation. However, the technique in [1] requires much less compute so is able to run on a CPU.

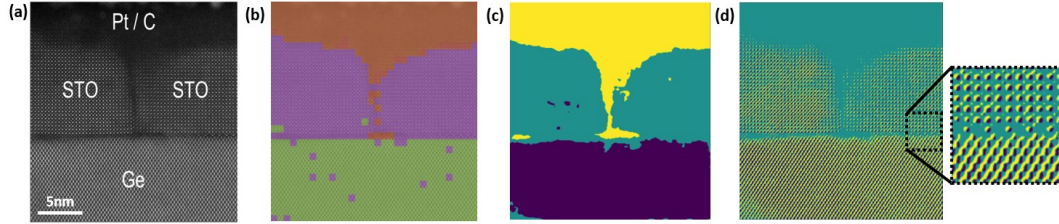


Figure 9: Comparison of the STEM data segmentation from [1] with the output of our unsupervised segmentation technique applied to the same STEM data. (a) Original 3042×3044 pixels STEM image of STO/Ge. (b) Segmentation of image from [1]. (a) and (b) are reproduced from [1] under a Creative Commons CC BY 4.0 license (<https://creativecommons.org/licenses/by/4.0/>). No changes were made. (c) Segmentation using technique from section 3.2 using a down sampled version that was 350×350 pixels. (d) Segmentation using technique from section 3.2. Image here was down sampled to 1500×1500 pixels.